Monitoring degradation mechanisms in PTB7:$PC_{71}BM$ photovoltaic cells by means of impedance spectroscopy

Belén Arredondo[a], María B. Martín-López[a], Beatriz Romero[a], Ricardo Vergaz[b], Pablo Romero-Gomez[c], and Jordi Martorell[c,d]

[a]Escuela de Ciencias Experimentales y Tecnología, Universidad Rey Juan Carlos, 28933, Móstoles (Madrid), Spain.

[b] Grupo de Displays y Aplicaciones Fotónicas GDAF-UC3M, Departamento de Tecnología Electrónica, Escuela Politécnica Superior, Universidad Carlos III de Madrid, 28911 Leganés (Madrid), Spain

[c]ICFO-Institut de Ciencies Fotoniques, Mediterranean Technology Park, 08860 Castelldefels (Barcelona), Spain.

[d]Departament de Fisica i Enginyeria Nuclear, Universitat Politècnica de Catalunya, Terrassa, Spain.

Abstract

We have used impedance spectroscopy technique to monitor degradation mechanisms in organic solar cells based on a blend of PTB7:$PC_{71}BM$. We have measured the impedance of the cell on a periodical basis for almost four months, and experimental data have been modelled using three different circuits. The evolution of the circuital parameters gives information about the device dynamical mechanisms. We have observed at high voltages a low frequency feature that is more pronounced along days of measurement. This low frequency arc has been associated to charge accumulation that is related to a worsening of charge extraction through the contacts. The simultaneous increase of recombination and low frequency resistances at high voltages (around V_{oc}) results in a decrease of the fill factor and therefore of the efficiency.

Keywords: Organic solar cells, impedance spectroscopy, monitoring degradation.

1. Introduction

During the last years, organic photovoltaic (OPV) has become a promising technology in the field of renewable energy [1-3]. Among all types of OPV, bulk heterojunction (BHJ) organic solar cells (OSCs) have become very popular due to the high efficiencies achieved using both small molecules [4] and polymers [5]. OSCs offer advantages over inorganic devices (both, silicon or III-V) such as lightweight, thinness, potential flexibility, transparency, low cost and low temperature fabrication techniques such as spin coating, spray coating, inkjet printing, etc. However, there are still some issues, such as device stability and life time that must be solved before OPV turns into a real alternative to inorganic devices [6].

Regarding materials, poly (3-hexylthiophene) P3HT and fullerene [6,6]-phenyl-C60 butyric acid methyl ester $PC_{60}BM$ blend has been the most studied and understood system, and it has achieved efficiencies up to 4 % [7]. This value has been far exceeded by using a new donor material: poly[[4,8-bis[2-ethylhexyl)-hexyl)oxy]benzo[1,2-b:5-b']dithiophene-2,6-diyl][3-fluoro-2-[(2-ethyl-hexyl)carbonyl]thieno[3,4-b] thiophenediyl]] (PTB7). Using this material blended with $PC_{71}BM$, a certified efficiency of 9.2 % has been obtained [5]. This improvement has been achieved thanks to: i) the absorption of PTB7 in the near infra-red region, ii) the proper energy level alignment with the work function of most used contacts, and iii) the high carrier mobility in this polymer. Besides, PTB7 is semitransparent, making it an ideal candidate for building integrated PV [8]. However, one of the main drawbacks of this technology is the poor device stability. Several works have been focused on this problem, in particular, the penetration of the oxygen and moisture into the active layer [9-13]. The fabrication of inverted poly(3,4-ethylenedioxylenethiophene):poly(styrenesulphonic acid) (PEDOT:PSS) free cells, avoids the etching of indium tin oxide (ITO) [14].

On the other hand, Impedance Spectroscopy (IS) technique is a valuable tool for obtaining information about carrier dynamics inside the device [15]. It has been used extensively in organic devices such as emitters [16] and OSCs [17-19]. It consists of superimposing a small voltage signal on a DC voltage. The frequency response of the electrical impedance (defined as the small signal voltage over the small signal current) provides information about material and device parameters such as dielectric constant, built-in voltage, acceptor impurity concentration, geometrical capacitance and mobility [20]. Carrier transport and recombination mechanisms can be identified in the IS spectra and times related to those processes (recombination and diffusion times) can be estimated [17, 20, 21]. It also provides information about the selectivity of the contacts [22, 23] and allows distinguishing between effects taking place in different parts of the device, such as the bulk, interfaces and electrodes [24]. In the last years this technique has been occasionally applied to study degradation mechanisms in OSCs. By comparing IS in fresh and aged devices, Zhao et al. determined that degradation processes take place at different interfaces (P3HT/PCBM and blend/electrode) [25]. Lin et al. performed a layer analysis using IS in dark conditions and obtained information about the changes taking place in device layers and interfaces during the degradation process [26]. By comparing IS before and after the degradation, Weerasinghe et al. conclude that degradation is due to the formation of an electron barrier at the electrode interface and not due to layer delamination [27]. Other works using impedance measurements revealed an increase of the transport resistance in aged devices that is correlated with an increase of defects that obstruct the efficient transport of carriers. Simultaneously, measurements showed an improvement of the electron contact selectivity due to a better covering of the cathode with fullerene molecules [28].

In this work we present a detailed degradation study by means of monitoring the impedance spectra of a non-encapsulated inverted OSC based on a blend of PTB7:$PC_{71}BM$ on a periodical basis for almost four months. The cell structure is ITO/ZnO/PTB7:$PC_{71}BM$/MoO3/Ag deposited onto glass substrate. Measurements have been performed in dark and under illumination at different bias voltages. Experimental data have been fitted with different equivalent circuits including constant phase (CPE) and Warburg elements.

Experimental details

ITO coated substrates were used as cathode. The ZnO layer was grown by sol-gel where the precursor solution was prepared according to [29]. Spin coating was performed at 6000 rpm during 60 seconds followed by a thermal annealing at 200^{o}C during 20 min in air. The active layer PTB7:$PC_{71}BM$ with a relation 1:1.5 was deposited by spin coating in a glovebox system yielding a thickness of 100 nm. A thermally evaporated thin film of MoO_3 (5 nm) was used as electron blocking layer (EBL). A 100 nm Ag layer was evaporated as anode. Devices were not encapsulated. Inset in Figure 1a shows a cross section scheme of the device.

The I-V characteristic was measured using an Abet Technologies Sun 3000 solar simulator calibrated with a monocrystal silicon reference cell (Rera Systems).

Impedance measurements were performed with a Solartron 1260 impedance analyzer. The cell was connected to the analyzer that fed the input signal, biasing the device at different DC levels and superimposing an alternating signal of sweeping frequency with amplitude 100 mV. Light measurements were performed illuminating the device with a conventional red LED (TLHR4400 from Vishay) since absorbance of PTB7:$PC_{71}BM$ films presents a maximum at 600 nm.

2. Results and Discussion

Figure 1(a) shows the I-V curve of a pristine device under illumination AM1.5 irradiation (100 mW/cm^2). Parameters of pristine solar cells are: J_{sc} = 13.26 mA/cm^2, V_{oc} = 0.75 V, FF = 73 % and efficiency (η) = 7.27 %. Inset depicts the layer structure of the inverted device where the Ag behaves as the anode contact, ITO is the cathode, ZnO is used as HBL (hole blocking layer) and MoO_3 as EBL. State of the art of inverted solar cells based on PTB7 with ohmic contacts for photogenerated charge collection presents efficiencies of 9.2 % and long-term ambient stability when devices are encapsulated in inert atmosphere [5].

The time evolution of the FF and the efficiency for the device are shown in Figure 1(b). The measured PV parameters were normalized to the corresponding initial values. In between measurements the cells were stored at ambient conditions in dark, which corresponds to ISOS-D-1 Shelf test at level 2, according to consensus stability testing protocols for OPVs [30]. The other parameters (J_{sc} and V_{oc}) remain constant until the efficiency drops to 40% of its initial value [31]. The evolution of the efficiency follows that of the FF until it reaches that value.

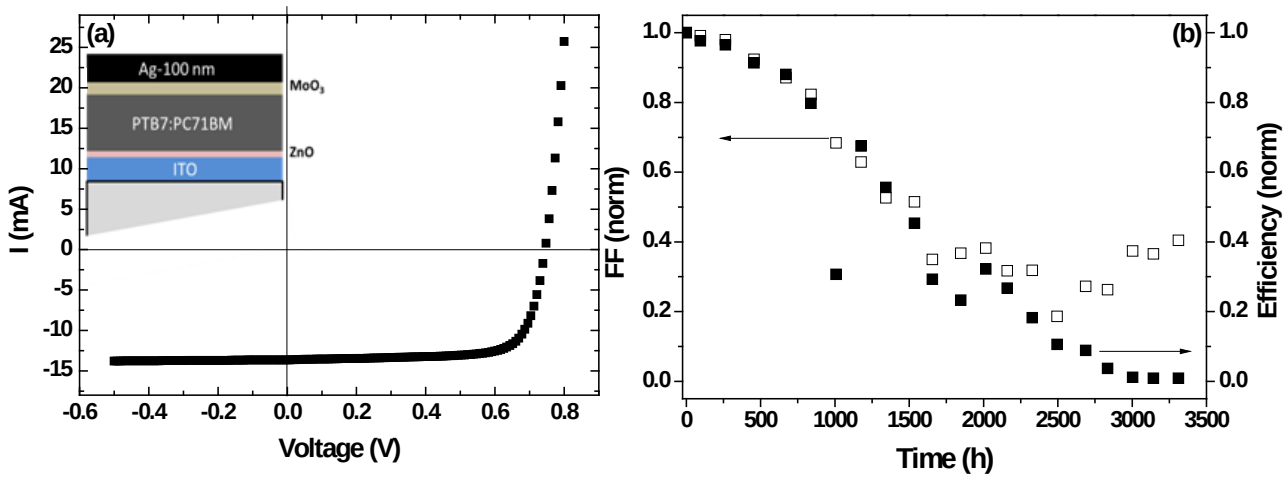

Figure 1. (a) I-V curve under 1 sun AM1.5 illumination of a fresh cell. Inset shows the device layer structure, (b) Evolution of the normalized FF and efficiency. The parameters are normalized to the respective value at t = 0h.

Figure 2(a) shows the impedance Cole-Cole diagram in dark conditions of the pristine device from 1 Hz to 1 MHz, at 0.2 and -2 V with no significant injected current. Experimental data (open symbols) resemble a depressed semicircle that has been modeled with the parallel R-CPE circuit shown in figure 3, named hereafter **Model A**. Solid lines of Figure 2(a) show the fit. The depressed semicircle is usually modeled with two or three parallel RC sets, each one related to a time constant of a dynamical process inside the cell [32]. In this work, attempts to describe it using RC sets have been unfruitful, and a distributed element resumed in CPE has been used, suggesting that the involved interfaces may have great porosity [15]. R_S is modeling wires and contacts, and R_P is the parallel combination of shunt and dynamical resistances. A constant phase element (CPE) is a non-ideal capacitor that models the non-homogeneous double-layer with $Z_{CPE}=1/(CPE_T(j\omega)^{CPE_P})$. Since all the fits leads CPE_P values ranging from 0.9 to 1, CPE will be approximated to a capacitor with CPE_T = C, the capacity value. The capacitance extracted from the fit to dark measurements at negative and sufficiently low bias that no charge is injected, follows a Mott-Schottky voltage dependence, related to the depletion capacitance at the cathode contact, whose expression is given by [20]:

$$C^{-2} = \frac{2(V_{bi} - V)}{A^2 e \varepsilon \varepsilon_0 N_A} \qquad (1)$$

where previous CPE_T = C, V_{bi} is the built-in potential required for flat band conditions at the cathode interface, N_A is the acceptor impurity density, A is the area (9.6 mm^2), V is the applied voltage and ε and ε_0 are the dielectric constant and vacuum permittivity respectively.

The dielectric constant is obtained from the geometrical capacitance (capacitance at reverse bias) as:

$$\varepsilon = \frac{CL}{A\varepsilon_0} \qquad (2)$$

with L being the active layer thickness, 100 nm, leading a value of 3.6, in agreement with [33]. Figure 2(b) shows the linear regression of equation (1) to the experimental data. The acceptor impurity density $N_A = 1.07x10^{17}$ cm^{-3}, and the built in potential V_{bi} = 0.52 V, have been calculated from the slope and the intercept with the X axis of the linear fit respectively.

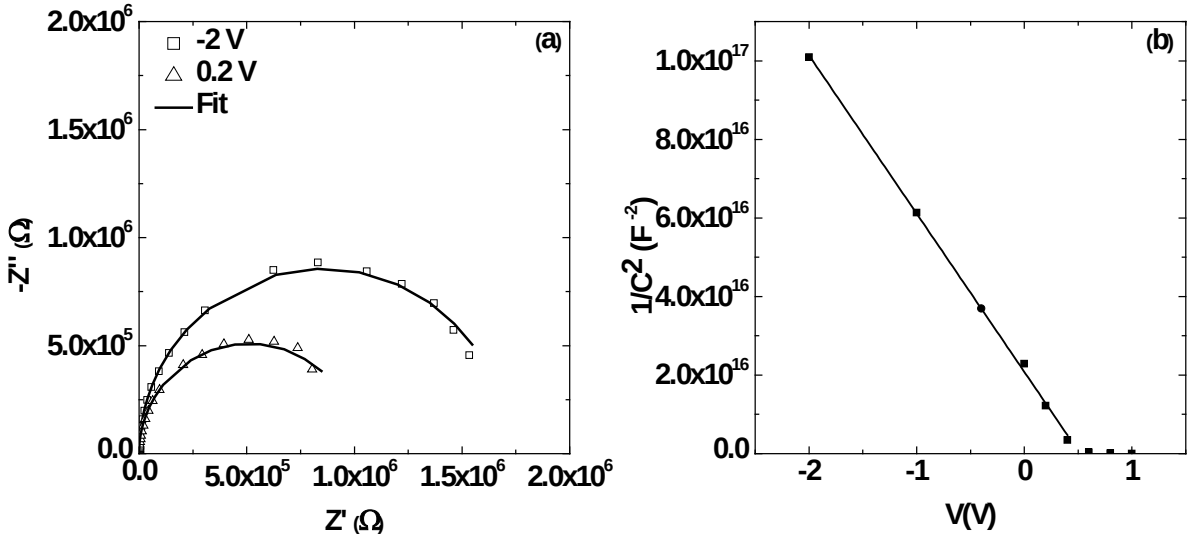

Figure 2. (a) Impedance spectra under dark conditions at two voltages. Solid lines show the fit with a parallel R-CPE circuit. (b) Mott-Schottky curve using capacitance values obtained from the fit using the circuit A of figure 3, where CPE_T = C.

Figure 4 depicts experimental impedance spectra under illumination at different bias voltages for fresh devices, ranging from 0 to 0.4 V in Fig. 4(a), and from 0.6 to 0.8 V in Fig. 4(b). Experimental data have been fitted using the equivalent circuits of figure 3. Model A has been used again for voltages below 0.6 V since spectra resemble one

semicircle as shown in figure 4(a). In this case, capacitance associated to the CPE element of model A is the chemical capacitance associated to the excess of charges in the device.

At voltages equal or above 0.6 V a new feature at low frequencies (right side of the Cole-Cole plot) appears. This tail has been modeled with: i) Warburg element (model B in figure 3) and ii) an extra R-CPE element (model C in figure 3). As it will be discussed later in the paper, the appearance of such a low frequency tail may be related to a charge accumulation inside the device (model C). However, the tail shape changes along time from a depressed semicircle to a line with slope under 45º. This low frequency feature time evolution can be associated to a Warburg phenomenon in which slow diffusion effects may be occurring (model B).

It is remarkable that both, CPE and Warburg elements, can be created from a transmission line of R-C elements, ensuring a unit repetition higher than 100. These distributed elements reproduce the spectra of the former non-ideal elements.

Figure 3 summarizes the three circuits used to model impedance spectra.

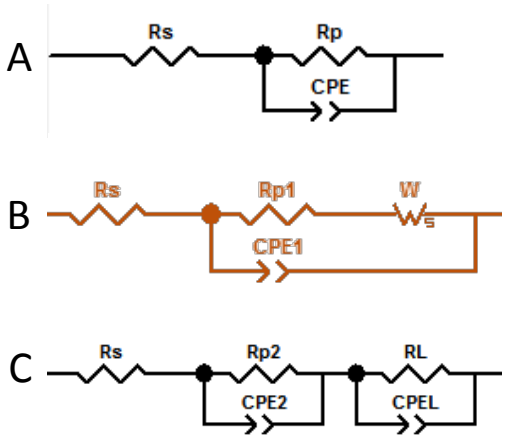

Figure 3. Circuit A has been used to fit impedance measurements below 0.6 V. Circuits B and C have been used to model impedance data from 0.6 up to 1V.

Model B consist of short circuit Warburg element [15] in series with the recombination resistance (here R_{P1}), all in parallel with a CPE (named here as CPE1), that reproduces the low frequency tail [31]. Warburg impedance can be defined as:

$$Zw = W_R \frac{\tanh\left(j\omega W_T\right)^{W_P}}{\left(j\omega W_T\right)^{W_P}} \quad (3)$$

where W_R is the Warburg resistance, W_T is a Warburg capacitance and W_P is a constant value in our case ranging from 0.3 to 0.5. Warburg element has been often found in literature in different devices, including dye solar cells [34-35].

Figure 4 (b) shows that both models B and C can accurately reproduce the experimental impedance spectra overlapping in the whole frequency range. We propose that the low frequency feature, modeled either the Warburg element (model B) or the extra R_L-CPE_L (model C), can be interpreted as a charge accumulation that cannot be effectively extracted through the contacts. It is worth pointing out that IS technique does not allow to determine in which electrode the charge accumulation takes place. Previous works report on charge accumulation at the ZnO interface but only when the cell is illuminated [36, 37]. In our case, the low frequency arc in the Nyquist plot occurs at high voltages (0.6 and 0.8 V), both in dark and light conditions, suggesting that the charge accumulation is not due to photo induced carriers but to the applied electric field. On the other hand, the anode is exposed to oxygen and water since devices are inverted and not encapsulated, suggesting that both slow diffusion and charge accumulation phenomena at the anode are not discarded scenarios. In summary, the low frequency arc in the Cole-Cole increases the device resistivity, worsening charge extraction and thus generating a charge accumulation effect.

It is remarkable that no transport resistance associated to diffusion mechanisms is needed to model the impedance spectra at high frequencies, implying that the mobility of the blend material is such that transport is not limiting conduction

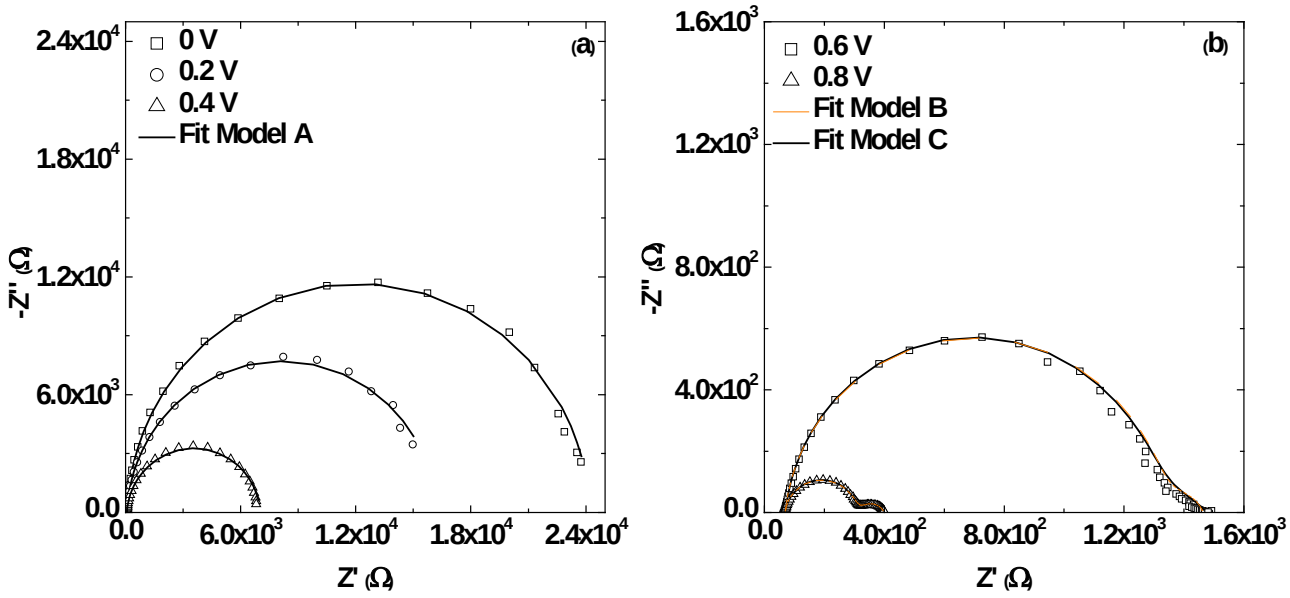

Figure 4. Impedance spectra of fresh devices under illumination at several voltages. Solid lines show the fit to the circuits of figure 3.

Figure 5 shows the parameters extracted from the previous fits at voltages ranging from 0 to 1 V. Figures 5(a) and (b) show the resistive parameters, and figures 5(c) and (d) the capacitive ones. Figure 5(a) shows that R_P, R_{P1} and R_{P2} follow the same trend with R_{P1} and R_{P2} overlapping at high voltages. These parallel resistances decrease with voltage, indicating an increase of charge recombination as expected.

Figure 5(c) shows the accurate match of $CPE1_T$ and $CPE2_T$ following the same trend as CPE, and increasing with voltage due to charge injection. At 0.6V the impedance spectra do not clearly show a low frequency semicircle but a tail causing a mismatch between $CPE1_T$ and $CPE2_T$. Models B and C are equivalent and lead to similar parameters when two arcs are clearly observed but differ at this transition voltage.

Concerning W_R and R_L shown in Figure 5(b), both parameters have similar values since they are both related to the low frequency arc diameter. Low frequency capacitors shown in Figure 5d do not present the same values since they are not equivalent from a circuital point of view. Even though the low frequency resistances (W_R and R_L)

decrease with voltage, this does not mean that the charge accumulation effect decreases. These parameters have to be regarded in comparison to the parallel resistances (R_{P1} and R_{P2}) associated to charge recombination. In order to study the influence of charge accumulation resistance in the overall cell impedance, the ratio W_R/R_{P1} has been calculated obtaining 0.12 and 0.42 for 0.6 V and 0.8 V respectively. This suggests that the influence of charge accumulation phenomenon at the interface increases with voltage as was expected.

Although at first glance the low frequency arc may also be attributed to traps states present in the organic layer, we have discarded this hypothesis since traps would respond to the low frequency signal at low voltages, when traps begin to fill. However, the low frequency arc only appears in the Nyquist plot at high voltages (see Figure 4b) when there is a strong charge injection. In this situation, the high current flowing through the device would strongly affect the trap occupancy function (trap states would be filled) avoiding the small signal to activate the trapping-detrapping process and thus suppressing the trap response. This dismisses trap mechanisms and supports the hypothesis of charge accumulation [38].

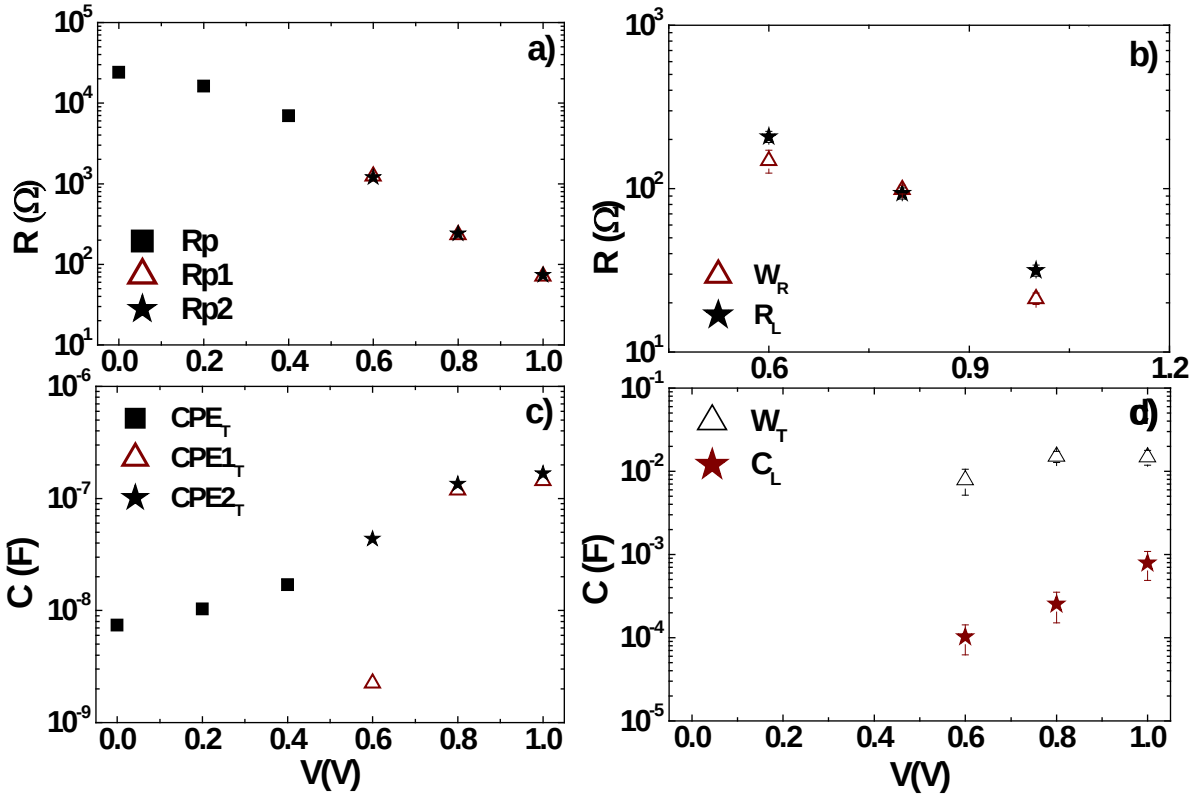

Figure 5. Parameters obtained from the fits of figure 4 using models of figure 3. Model A, B and C parameters are plotted with squares, hollow triangles and stars respectively. (a) Parallel resistance, R_P. (b) Warburg resistance and R_L associated to low frequencies (c) CPE_T (=C) attributed to the main semicircle in the Cole-Cole plot. (d) CPE_L (= C_L) and Warburg capacitive (=W_T) parameter related to the low frequency feature. Error bars are included in figures (b) and (d), in figures (a) and (c) the error bar is within the symbol size.

In an attempt to check the variations of the previous parameters with time, Figure 6 shows selected impedance spectra for the 107 days of tracking. Although some fluctuations can be observed, the overall trend is that the magnitude of the impedance increases due to the raise of R_P (the right intercept of the depressed semicircle with the X axis). Figure 6b shows the evolution of impedance spectra with time at 0.8V, depicting that from a circuital point of view both models B and C can accurately reproduce the low frequency feature. In addition, Figure 6b shows an increase with time of the low frequency arc suggesting that the effect of charge accumulation is more pronounced with time. This effect is related to cell degradation, since at high voltages and low frequency, an increase of the overall resistance implies that the I-V curve flattens diminishing the slope and thus fill factor.

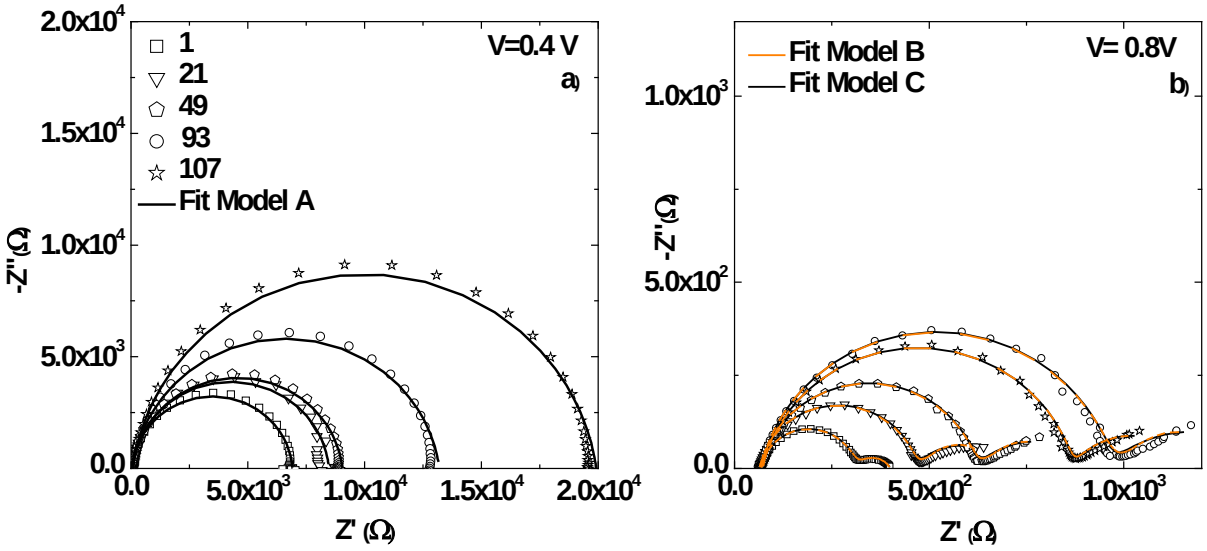

Figure 6. a) Evolution of impedance spectra for 107 days at two voltages 0.4 V and b) 0.8 V. Solid lines show the fit to models A, B and C.

Figure 7a shows that the parallel resistance at 0.4 V remains quasi-stable until the last days of measurement that slightly increases with time, suggesting that the bulk layer degrades leading eventually to permanent device failure, as has been previously observed by [26, 27].

Figures 7b and 7d show an increase with time of the low frequency resistance (R_L and W_R) and low frequency capacitances (W_T and C_L) respectively. Both trends indicate an enhancement in the charge accumulation, increasing the resistive effect at the contact, thus hindering charge extraction through the electrodes and ultimately contributing to device degradation. This fact is confirmed by the slight increase of the chemical capacitance shown in Figure 7c. From a circuital point of view, the sum of R_P and R_L (or W_R), neglecting R_S, represents the inverse of the I-V slope. Thus, at 0.8 V (around V_{oc}), a simultaneous increase of R_P and W_R with time implies a decrease of such slope, and consequently a decrease in FF and thus efficiency, which is in agreement with Figure 1b.

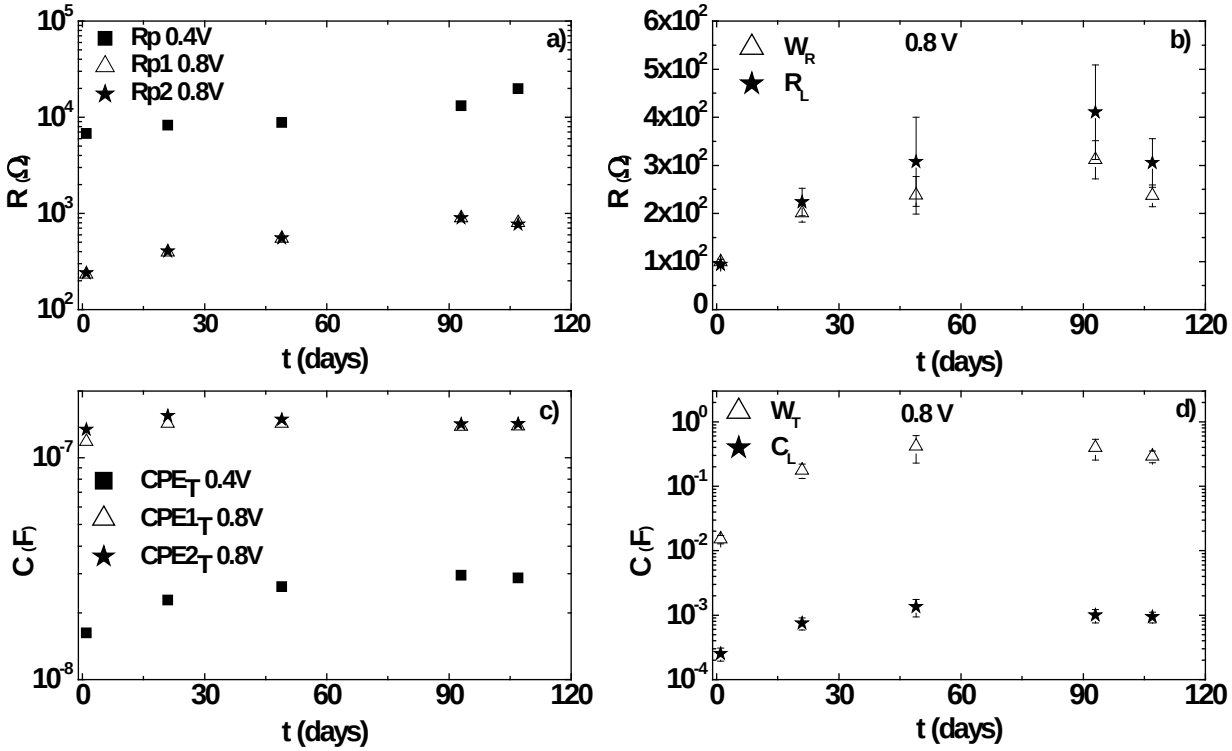

Figure 7. Evolution of parameters obtained from the fit of figure 6 for 107 days at V = 0.4 and 0.8 V. Model A, B and C parameters are plotted with squares, hollow triangles and stars respectively. (a) Parallel resistance, R_P; (b) Resistance associated to the low frequency feature; (c) Capacitance CPE_T; (d) Capacitance associated to low frequencies. Error bars are included in figures (b) and (d), in figures (a) and (c) the error bar is within the symbol size.

Figure 8 shows the carrier density extracted from the integral of the chemical capacitance versus time. As mentioned before, the impedance spectra do not show a conduction limiting effect associated to charge diffusion mechanism. The increase of carrier density again ratifies the hypothesis that charges cannot be efficiently extracted through the contacts, possibly due to the charge accumulation at the electrodes. After 20 days of measurement the excess of carriers within the cell saturates. Moreover, some authors have also suggested the formation of a metal-oxide layer due to corrosion of metal electrode surface that can act as a charge-transport barrier [39].

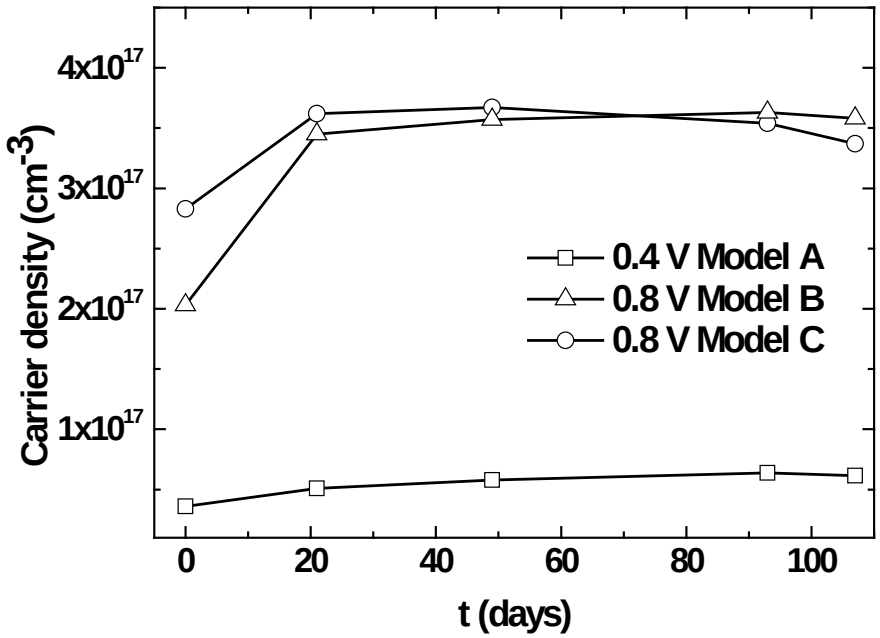

Figure 8. Carrier density extracted from the integral of chemical capacitance (CPE_T) vs time at 0.4 and 0.8 V.

3. Conclusions

We have measured impedance spectra of non-encapsulated inverted organic solar cells based on PTB7:$PC_{71}BM$ for almost four months in order to study degradation. Low voltage measurements have been successfully fitted using a classic equivalent circuit, with a contact resistance R_S in series with a parallel set of a mainly capacitive constant phase element CPE, and a carrier recombination resistance R_P. However, a new feature appears at high voltages and low frequencies that has been accurately modeled with two different equivalent circuits, one including a Warburg element and the other one using an extra R-CPE. The low frequency feature suggests charge accumulation effects at the electrodes that ultimately results in a worsening of charge extraction, due to the incorporation of oxygen and water through the anode. Moreover, the parallel resistance associated to the active blend increases with time, indicating a worsening of conduction in the bulk, and thus a cell degradation. The increase of the overall resistance (R_P+R_L)

with time at high voltages is in agreement with the diminishing of the I-V slope and the corresponding decrease of the fill factor.

Acknowledgements

This work was supported by the Ministerio de Economía y Competitividad with the project TEC2013-47342-C2-1-R, and the R&D Program SINFOTON S2013/MIT-2790 of the Comunidad de Madrid. We acknowledge support from the EC under the project Solprocel with grant number No. 604506.

References

[1] G. Li , R. Zhu, Y. Yang, Polymer Solar Cells, Nat. Photonics 6, (2012) 153–161.

[2] M. Wright, A. Uddin, Organic-inorganic hybrid solar cells: A comparative review, Sol. Energy Mater. Sol. Cells 107 (2012) 87–111.

[3] N. Espinosa, M. Hosel, D. Angmo, F. C. Krebs, Solar cells with one-day energy payback for the factories of the future. Energy Environ. Sci. 5 (2012) 5117–5132

[4] V. Gupta, A. K. K. Kyaw, D. H. Wang, S. Chand, G. C. Bazan, A. J. Heeger, Barium: An Efficient Cathode Layer for Bulk-Heterojunction Solar Cells, Nat. Sci. Rep. 3 (2013) 1965.

[5] Z. He Z, C. Zhong, S. Su, M. Xu, H. Wu, Y. Cao, Enhanced power-conversion efficiency in polymer solar cells using an inverted device structure. Nat. Photonics 6 (2012) 591–595.

[6] C. J. Brabec, S. Gowrisanker, J. J. M. Halls, D. Laird, S. J. Jia, S. P. Williams, Polymer–Fullerene Bulk-Heterojunction Solar Cells. Adv. Mater. 22 (2010) 3839-3856.

326 [7] A. J. Moule, K. Meerholz, Controlling Morphology in Polymer–Fullerene
327 Mixtures, Adv. Mater. 20 (2008) 240-245.

328 [8] R. Betancur , P. Romero-Gomez , A. Martinez-Otero , X. Elias , M. Maymó , J.
329 Martorell, Transparent polymer solar cells employing a layered light-trapping
330 architecture, Nat. Phot. 7 (2013), 995-1000.

331 [9] M. Jørgensen, K. Norrman, S. A. Gevorgyan, T. Tromholt, B. Andreasen, F.C.
332 Krebs, Stability of Polymer Solar Cells. Adv. Mater. 24 (2012) 580-612.

333 [10] C. H. Peters, I. T. Sachs-Quintana, J. P. Kastrop, S. Beaupre, M. Leclerc, MD
334 McGehee, High Efficiency Polymer Solar Cells with Long Operating Lifetimes. Adv.
335 Energy Mater. 1 (2011) 491-494.

336 [11] D. Angmo, S. A. Gevorgyan, T.T. Larsen-Olsen,R. R. Søndergaard; M. Hösel;
337 M. Jørgensen; R. Gupta; G. U. Kulkarni; F. C. Krebs. Scalability and Stability of Very
338 Thin, Roll-to-Roll Processed, Large Area, Indium-Tin-Oxide Free Polymer Solar Cell
339 Modules. Org. Electron. 14 (2013) 984-994.

340 [12] T. Y. Chu, S. W. Tsang, J. Zhou, P.G. Verly, J. Lu, S. Beaupre, M. Leclerc, Y.
341 Tao, High-efficiency inverted solar cells based on a low bandgap polymer with
342 excellent air stability. Sol. Energy Mater. Sol. Cells 96 (2012) 155-159.

343 [13] N. Espinosa, R. Garcıa-Valverde, A. Urbina, F. C. Krebs, A life cycle analysis of
344 polymer solar cell modules prepared using roll-to-roll methods under ambient
345 conditions. Sol. Energy Mater. Sol. Cells 95 (2011) 1293-1302.

[14] E. Litzov, C. J. Brabec, Development of Efficient and Stable Inverted Bulk Heterojunction (BHJ) Solar Cells Using Different Metal Oxide Interfaces. Mater. 6 (2013) 5796-5820.

[15] E. Barsoukov, J. R. MacDonald, Impedance Spectroscopy. Theory, Experiment, and Applications. Ed. Wiley-Interscience (2005).

[16] L. S. C. Pingree, B. J. Scott, M. T. Russel, T. J. Marks, M. C. Hersam, Negative capacitance in organic light-emitting diodes, Appl. Phys. Lett. 86 (2005) 073509.

[17] G. Perrier, R. Bettignies, S. Berson, N. Lemaitre, G. Guillerez, Impedance spectrometry of optimized standard and inverted P3HT-PCBM organic solar cells. Sol. Energy Mater. Sol. Cells 101 (2012) 210-266

[18] T. Kuwabara, C. Iwata, T. Yamaguchi, K. Takahashi, Mechanistic Insights into UV-Induced electron Transfer from PCBM to Titanium Oxide in Inverted-Type Organic Thin Film Solar Cells Using AC Impedance Spectroscopy, ACS Appl. Mater. Interfaces. 2 (2010) 2254-2260.

[19] G. García-Belmonte, A. Guerrero, J. Bisquert, Elucidating Operating Modes of Bulk-Heterojunction Solar Cells from Impedance Spectroscopy Analysis, J. Phys. Chem. Lett. 4 (2013) 877-886.

[20] G. García-Belmonte, A. Munar, E. M. Barea, J. Bisquert, I. Ugarte, R. Pacios, Charge carrier mobility and lifetime of organic bulk heterojunctions analyzed by impedance spectroscopy, Org. Electron. 9 (2008) 847-851.

[21] G. García-Belmonte, P. P. Boix, J. Bisquert, M. Sessolo, H. J. Bolink, Simultaneous determination of carrier lifetime and electron density-of-states in

368 P3HT:PCBM organic solar cells under illumination by impedance spectroscopy, Sol.
369 Energy Mater. Sol Cells 94 (2010) 366-375.

370 [22] A. Guerrero, N. F. Montcada, J. Ajuria, I. Etxebarria, R. Pacios, G. García-
371 Belmonte, E. Palomares, Charge carrier transport and contact selectivity limit the
372 operation of PTB7-based organic solar cells of varying active layer thickness, J. of
373 Mater. Chem. A 1 (2013) 12345-12354.

374 [23] I. Etxebarria, A. Guerrero, J. Albero, G. García-Belmonte, E. Palomares, R.
375 Pacios, Inverted vs standard PTB7:PC70BM organic photovoltaic devices. The benefit
376 of selective and extracting contacts in device performance, Organic Electronics 15
377 (2014) 2756-2762.

378 [24] B. Ecker, H. J. Egelhaaf, R. Steim, J. Parisi and E. von Hauff, Understanding S-
379 shaped Current-Voltage Characteristics in Organic Solar Cells Containing a TiOx
380 Interlayer with impedance Spectroscopy and Equivalent Circuit Analysis, J. Phys. Chem
381 C 116 (2012) 16333-16337.

382 [25] C. X. Zhao, L. L. Deng, M. Y. Ma, J. R. Kish and G. Xu, Multiple-interface
383 tracking of degradation process in organic photovoltaics, AIP Advances 3 (2013)
384 102121.

385 [26] K. Lin, Z. Nan, L. Edna, W. Rui, K. Z. Ming, W. Xizu, L. Bin, Organic
386 photovoltaic initial stage degradation analysis using impedance spectroscopy, Synthetic
387 Metals 202 (2015) 63-67

388 [27] H. C. Weerasinghe, S. E. Watkins, N. Duffy, D. J. Jones, A. D. Scully, Influence
389 of moisture out-gassing from encapsulant materials on the lifetime of organic solar
390 cells, Sol. Energy Mater. Sol Cells 132 (2015) 485-491.

391 [28] A. Guerrero, M. Pfannmöller, A. Kovalenko, T. S. Ripolles, H. Heidari, S. Bals,
392 L-D Kaufmann, J. Bisquert and G. García-Belmonte, Nanoscale mapping by electron
393 energy-loss spectroscopy reveals evolution of organic solar cell contact selectivity,
394 Organic Electronics 16 (2015) 227-233.

395 [29] F. F. Pastorelli, P. Romero-Gomez, R. Betancur, A. Martinez-Otero, P. Mantilla-
396 Perez, N. Bonod, J. Martorell, Solar Cells: Enhanced Light Harvesting in
397 Semitransparent Organic Solar Cells using an Optical Metal Cavity Configuration. Adv.
398 Energy Mater. 5 (2015) 1400614.

399 [30] M. O. Reese, et al., Consensus stability testing protocols for organic photovoltaic
400 materials and devices, Sol. Energy Mater. Sol. Cells 95 (2011) 1253-1267.

401 [31] P. Romero-Gomez, R. Betancur, A. Martinez-Otero, X. Elias, M. Mariano, B.
402 Romero, B. Arredondo, R. Vergaz, J. Martorell, Enhanced stability in semi-transparent
403 PTB7/PC71BM photovoltaic cells, Sol. Energy Mater. Sol. Cells, 137 (2015) 44-49.

404 [32] A. Guerrero, H. Heidari, T. S. Ripolles, A. Kovalenko, M. Pannmöller, S. Bals,
405 L-D. Kauffmann, J. Bisquert, G. García-Belmonte, Self Life Degradation of Bulk
406 Heterojunction Solar Cells: Intrinsic Evolution of Charge Transfer Complex, Adv.
407 Energy Mater. 5 (2015) 1401997.

408 [33] J. Singh, M. R. Narayan, Optimizing the Design of Flexible PTB7:PC71BM
409 Bulk-Heterojunction and P3HT:SiNW Hybrid Organic Solar Cells. Nanosci. &
410 Technol. 1 (2014).

411 [34] E. Guillén, J. Idigoras, T. Berger, J. A. Anta, C. Fernandez-Lorenco, R.
412 Alcántara, J. Navas, J. Martin-Calleja, ZnO-based dye solar cell with pure ionic-liquid

413 electrolyte and organic sensitizer: the relevance of the dye–oxide interaction in an ionic-
414 liquid medium, Phys. Chem. Chem. Phys. 13 (2011) 207-213.

415 [35] C. P. Lee, M. H. Yeh, R. Vittal, K. C. Ho, Solid-state dye-sensitized solar cell
416 with a charge transfer layer comprising two ionic liquids and a carbon material. J.
417 Mater. Chem. 21 (2011) 15471-15478.

418 [36] K. Norrman, M. V. Madsen, S. A. Gevorgyan, F. C. Krebs, Degradation patterns
419 in water and oxygen of an inverted polymer solar cell, J. Am. Chem. Soc. 132 (2010)
420 16883.

421 [37] M. V. Madsen, K. Norrman, F. C. Krebs, Oxygen-and water-induced degradation
422 of an inverted polymer solar cell: the barrier effect, J. Photon. Energy 1 (2011) 011104.

423 [38] L. Burtone, D. Ray, K. Leo, M. Riede, Impedance model of trap states for
424 characterization of organic semiconductor devices, J. App. Phys. 111 (2012) 064503.

425 [39] F. C. Krebs, Degradation and stability of polymer and organic solar cells, Sol
426 Energy Mater. Sol. Cells 92 (2008) 685.